Volume 1 | Number 1 | Jan 2013 | Pages 1–100

Nanoscale

www.rsc.org/nanoscale

ROYAL SOCIETY OF CHEMISTRY

ROYAL SOCIETY OF CHEMISTRY

www.rsc.org/nanoscale

Co(OH)$_2$/RGO/NiO Sandwich-Structured Nanotube Arrays with Special Surface and Synergistic Effects as a High-Performance Positive Electrode for Asymmetric Supercapacitor

Han Xu, Chi Zhang, Wen Zhou, and Gao-Ren Li*

MOE Laboratory of Bioinorganic and Synthetic Chemistry, KLGHEI of Environment and Energy Chemistry, School of Chemistry and Chemical Engineering, Sun Yat-sen University, Guangzhou 510275, China

*E-mail: ligaoren@mail.sysu.edu.cn

ABSTRACT

High power density, high energy density and excellent cycling stability are the main requirements for high-performance supercapacitors (SCs) that will be widely used for portable consumer electronics and hybrid electric vehicles. Here we investigate a novel type of hybrid Co(OH)$_2$/reduced graphene oxide (RGO)/NiO sandwich-structured nanotube arrays (SNTAs) as positive electrodes for asymmetric supercapacitors (ASCs). The synthesized Co(OH)$_2$/RGO/NiO SNTAs exhibit significantly improved specific capacity (~1470 F·g^{-1} at 5 mV·s^{-1}) and excellent cycling stability with ~98% C_{sp} retention after 10,000 cycles because of the fast transport and short diffusion paths for electroactive species, high utilization rate of electrode materials, and special synergistic effects among Co(OH)$_2$, RGO, and NiO. The high-performance ASCs are assembled basing on Co(OH)$_2$/RGO/NiO SNTAs as positive electrodes and active carbon (AC) as negative electrodes, and they exhibit high energy density (115 Wh·kg^{-1}), high power density (27.5 kW·kg^{-1}) and excellent cycling stability (less 5% C_{sp} loss after 10,000 cycles). This study shows an important breakthrough in the design and fabrication of mulit-walled hybrid nanotube arrays as positive electrodes for ASCs.

1. INTRODUCTION

The ever-growing energy demand has greatly stimulated recent research on exploiting high performance energy-storage devices.[1-2] Supercapacitors (SCs), also known as electrochemical capacitors or ultracapacitors, have been considered as one of the most promising energy-storage devices and they can offer a number of potentially high-impact characteristics including fast charging and discharging within seconds (i.e., fast response time), high power density (1~2 orders of magnitude higher than that of batteries), superior cycle lifetime (2~3 orders of magnitude better than that of batteries), and high reliability.[3-6] SCs can be utilized in a variety of applications ranging from portable consumer electronics to hybrid electric vehicles and to large industrial scale power and energy management.[7-10] Unfortunately, the practical applications of SCs are largely hindered by the low energy density and mediocre cycling stability because of the lack of high-performance electrode materials at a reasonable cost.[11-13] For example, the specific capacitance (C_{sp}) of carbon-based electrode materials is generally low.[14] The cycling stability of transition metal oxide and conducting polymer electrodes is usually less satisfactory.[15-18] Therefore, the development of SCs with high energy density and superior cycling durability is urgent and important.

Transition metal oxides, hydroxides, and their composites are being widely explored for SCs with increased capacity and energy density because of their high capacitance, low cost and low toxicity.[19-21] Among various metal oxides, NiO is a good candidate owing to its high C_{sp}, low cost, natural abundance, and different oxidation states of Ni.[22] Metal hydroxide $Co(OH)_2$ is also a good pseudocapacitive candidate and it has attracted much interest in recent years because of their layered structure with large interlayer spacing, good reversibility, low cost, high capacitance and well-defined electrochemical redox activity.[23] However, the electrode composed of above single material usually can not fulfill the requirements of future electrical energy storage devices due to the inherent material limitations such as low conductivity, low energy density and poor cycle stability during charge/discharge processes.[24-26] Recently, the hybrid electrode materials have attracted great attention for electrochemical energy storage because of the combining unique properties of individual materials with synergistic effects, realizing the

full potential of electrode materials in terms of performance.[27-31] In order to realize the practical

applications of high-performance SCs, tremendous efforts have been devoted to rational synthesis of

orderly hybrid materials, such as hybrid nanotube arrays (NTAs), because of their fascinating synergetic

properties, multifunctionalities and fast electron and ion transmissions.[32-36] However, the fabrication of

multi-layered hybrid NTAs electrodes still remains a huge challenge for SCs.

   Here we realize the design and synthesis of $Co(OH)_2$/reduced graphene oxide (RGO)/NiO sandwich-

structured nanotube arrays (SNTAs). Combining NiO and $Co(OH)_2$ with RGO that has extraordinary

electrical property and unusual mechanical strength to form multi-layered nanotube arrays will be an

efficient route for the performance enhancement of SCs. Such unique SNTAs architecture will provide

numerous channels for the access of electrolyte, high utilization rate of electrode material, high electrical

conductivity of electrode, and synergistic effects among $Co(OH)_2$, NiO and RGO. Electrochemical

measurements demonstrate that the $Co(OH)_2$/RGO/NiO SNTAs exhibit high C_{sp} ($\sim$1470 F·g^{-1} at 5 mV·s^{-1}),

superior rate capability, and excellent cycling stability. Furthermore, the high-performance asymmetric

supercapacitors (ASCs) were assembled by using $Co(OH)_2$/RGO/NiO SNTAs as positive electrodes and

active carbon (AC) as negative electrodes and the devices exhibited high energy density (115 Wh·kg^{-1}),

high power density (27.5 kW·kg^{-1}), and excellent cycling stability (less 5% C_{sp} loss after 10, 000 cycles).

This work constitutes the first demonstration of using $Co(OH)_2$/RGO/NiO SNTAs as high-performance

positive electrodes for ASCs.

2. EXPERIMENTAL SECTION

Synthesis of $Co(OH)_2$/RGO/NiO sandwich-structured nanotube arrays (SNTAs). All chemical reagents

were analytical (AR) grade. Electrochemical synthesis was performed in a simple three-electrode electrolytic

cell via galvanostatic electrodeposition, and a graphite electrode was used as the counter electrode (spectral

grade, 1.8 cm^2). The saturated calomel electrode (SCE) was used as the reference electrode, which was

connected to the cell with a double salt bridge system. The NiO/RGO/$Co(OH)_2$ SNTAs were fabricated using

the following procedures:

1) ZnO nanorod array template was electrodeposited in a solution of 0.01 mol·L^{-1} $Zn(NO_3)_2$ +0.05 mol·L^{-1}

NH_4NO_3 at a current density of 0.5 mA·cm^{-2} at 70 $^{\circ}$C for 90 min. Ti plates (99.99%, 1.5 cm^2) were used as the substrate for electrodeposition, which were prepared using the following steps before each experiment: first, they were polished by SiC abrasive paper with coarseness ranging from 300 to 800 grits; then, they were dipped in HCl solution (5%) for 10 min, rinsed with acetone in an ultrasonic bath for 5 min, and finally washed with distilled water.

2) ZnO/Co(OH)$_2$ core-shell nanorod arrays (NRAs) were prepared by the electrodeposition of Co(OH)$_2$ onto the surfaces of ZnO nanorods in a solution of 0.002 mol·L^{-1} Co(NO$_3$)$_2$ at a current density of 0.5 mA·cm^{-2} at 70 $^{\circ}$C for 1.0 min.

3) RGO layers were electrodeposited on the surfaces of ZnO/Co(OH)$_2$ NRAs to form ZnO/Co(OH)$_2$/RGO NRAs in a solution of 0.01 g·L^{-1} graphere oxide + 0.5 mol·L^{-1} Na$_2$SO$_4$ by galvanostatic electrolysis at 2.0 mA·cm^{-2} for 1.5 min at 25 °C.

4) The NiO layers were further electrodeposited onto the surfaces of ZnO/Co(OH)$_2$/RGO NRAs to form ZnO/Co(OH)$_2$/RGO/NiO NRAs in a solution of 0.01 mol·L^{-1} Mn(CH$_3$COO)$_2$ + 0.02 mol·L^{-1} NH$_4$NO$_3$ + 10% DMSO at a current density of 0.2 mA·cm^{-2} at 70 $^{\circ}$C for 8 min.

5) The synthesized ZnO/Co(OH)$_2$/RGO/NiO NRAs were immersed in a 5% NH$_3$·H$_2$O solution for 2 h to completely remove the ZnO nanorod array template, and accordingly the Co(OH)$_2$/RGO/NiO SNTAs were finally fabricated. The fabricated Co(OH)$_2$/RGO/NiO SNTAs were washed with doubly deionized H$_2$O several times.

Characterizations of Co(OH)$_2$/RGO/NiO SNTAs. The morphologies of the synthesized Co(OH)$_2$/RGO/ NiO SNTAs were characterized using a field emission scanning electron microscope (SEM, FEI, Quanta 400), a transmission electron microscope (TEM, JEM-2010HR) and a high-angle annular dark-field scanning TEM (HAADF-STEM, FEI Tecnai G2 F30). The chemical composition of the Co(OH)$_2$/RGO/NiO SNTAs was characterized by energy-dispersive X-ray spectroscopy (EDS, INCA 300) and X-ray photoelectron spectroscopy (XPS, ESCALAB 250). All XPS spectra were corrected using the C 1s line at 284.6 eV. Curve fitting and background subtraction were used. The samples were also characterized by Brunauer, Emmett, and Teller (BET) nitrogen sorption surface area measurements (Micromeritics ASAP 2010). Specific surface areas of the samples were calculated by the Brunauer-Emmett- Teller (BET) method.

Electrochemical characterizations: Electrochemical measurements of Co(OH)$_2$/RGO/NiO SNTAs were

carried out in a standard three-electrode electrolytic cell in $1.0 \ mol \cdot L^{-1}$ KOH aqueous solution. A graphite electrode was used as a counter electrode. A saturated calomel electrode (SCE) was used as the reference electrode. The working electrode was impregnated with the electrolyte for 30 min to ensure the composite electrode was thoroughly wet and then actived in small current with chronopotentiometric. Cyclic voltammometry and chronopotentiometric measurements were performed on a CHI 760 D electrochemical work-station (CH instruments, Inc.) to determine the electrochemical properties. The average specific capacitance (C_{sp}) determined from the cyclic voltammograms (CVs) were calculated according to Eq. (1):

$$C_{sp} = \frac{1}{w\Delta V} \int_y^x i\,dt \qquad (1)$$

Where i, ΔV and w were the current (mA), the voltage range of one scanning segment (V), and weight of electrode material (mg) (the mass loading is 0.20 mg), respectively. The C_{sp} was also calculated from the chronopotentiometric curves according to Eq. (2).

$$C_{sp} = \frac{I\Delta t}{w\Delta V} \qquad (2)$$

Where I was the charge/discharge current, Δt was the time for a full charge or discharge, w was the mass of the active electrode material, and ΔV was the voltage change after a full charge/discharge.

Asymmetric supercapacitors (ASCs): ASCs were assembled using $Co(OH)_2$/RGO/NiO SNTAs (0.20 mg) as positive electrodes, the active carbon (AC) (0.86 mg) as negative electrodes. The mass ratio between the positive and negative electrode is obtained via following equation: $m_+/m_- = C_-V_-/C_+V_+$ (C_+ and C_- is the C_{sp} of $Co(OH)_2$/RGO/NiO SNTAs and AC electrodes, respectively. V_+ and V_- is the voltage range of one scanning segment of $Co(OH)_2$/RGO/NiO SNTAs and AC electrodes, respectively). The TF45 (NKK) membrane was used as separators. The negative electrode was prepared as follows: firstly, the AC, acetylene black and poly-tetrafluoroethylene (PTFE) powers with mass proportions (%) of 80:10:10 were dispersed in 1-Methyl-2-pyrrolidinone (NMP) to produce a homogeneous paste by magnetic stirring. Then the resulting mixture was coated onto nickel foam substrate ($1.0 \ cm \times 3.0 \ cm$) by a spatula. Finally, the fabricated electrode was pressed and then dried at 120 ^{0}C for 24 h. The assembled ASCs were measured with a two-electrode system in $1.0 \ mol \cdot L^{-1}$ KOH aqueous solution. Cyclic voltammometry and chronopotentiometric measurements were performed in a two-electrode electrolytic cell on a CHI 760 D electrochemical workstation (CH instruments, Inc.) to determine the electrochemical performance of ASCs. The energy density and power density is calculated via Eqs. (3) and (4), respectively.

$$d_e = \frac{1}{2} C_{sp} (\Delta V)^2 \tag{3}$$

$$d_p = \frac{d_e}{\Delta t} \tag{4}$$

3. RESULTS AND DISCUSSION

The details of the fabrication of Co(OH)$_2$/RGO/NiO SNTAs are described in the Experimental Section. SEM image of the fabricated Co(OH)$_2$/RGO/NiO SNTAs is shown in Figure 1a, which shows the nanotube arrays are successfully fabricated and the nanotubes are separate from each other. The diameters of Co(OH)$_2$/RGO/NiO nanotubes are about 500 nm as shown in Figure 1a and their lengths are about 6.0 μm as shown in the sectional view in the inset in Figure 1a. The advantages of Co(OH)$_2$/RGO/NiO SNTAs as electrode materials for SCs are illustrated in Figure 1b. Firstly, the hollow structures of nanotubes and large open space among the neighboring nanotubes in Co(OH)$_2$/RGO/NiO SNTAs will provide three-dimensional (3D) space for transmission of ions throughout electrode, and accordingly the electroactive species can easily diffuse into the inside of electrode and the inner material of electrode can efficiently participate in the electrochemical reactions. Secondly, the Co(OH)$_2$/RGO/NiO SNTAs will provide rich heterogeneous interfaces, which is highly propitious to enhance the synergistic effects among Co(OH)$_2$, NiO, and RGO and subsequently can promote supercapacitive performance. Thirdly, as high conductivity of RGO, the Co(OH)$_2$/RGO/NiO SNTAs can overcome the poor electrical conductivity of Co(OH)$_2$ and NiO and accordingly will own advisable electrical conductivity to promote electrochemical reactions and electron transmission. In addition, the fabricated Co(OH)$_2$/RGO/NiO SNTAs own strong frame construction and can effectively resist Ostwald ripening and coalescence of electrode materials and will well promote elecrochemical performance and cycle stability. To investigate the distribution states of Co(OH)$_2$, NiO, and RGO, EDS mappings are carried out the surface of Co(OH)$_2$/RGO/NiO SNTAs. The typical partical surface of Co(OH)$_2$/RGO/NiO SNTAs is shown in Figure 1c, and accordingly EDS mappings were measured in this area. The elements of Co, Ni and C were uniformly dispersed as shown in Figure 1d, 1e, and 1f, respectively, indicating high dispersive Co(OH)$_2$, NiO and RGO. The Co : C : Ni atomic ratio in Co(OH)$_2$/RGO/NiO SNTAs is determined to be

48 : 6 : 46 by ICP-AES.

The structures of the Co(OH)$_2$/RGO/NiO SNTAs were further characterized by TEM, and the typical TEM image of Co(OH)$_2$/RGO/NiO SNTAs is shown in Figure 2a, which shows the Co(OH)$_2$/RGO/NiO SNTAs have diameters of about 500 nm and homogeneous wall thickness of about 50 nm. In order to prove the sandwich-like structures in the Co(OH)$_2$/RGO/NiO SNTAs, a magnified TEM image of the nanotube wall is shown in Figure 2b, which clearly shows the sandwich-like structures. The thicknesses of Co(OH)$_2$ layer, RGO layer, and NiO layer is ~23, ~17, and ~10 nm, respectively. HRTEM image of Co(OH)$_2$/RGO interface is shown in Figure 2d, which indicates that the Co(OH)$_2$ layer is polycrystalline structure and RGO layer is amorphous. HRTEM image of RGO/NiO interface is shown in Figure 2e, which indicates that the RGO layer is also amorphous and NiO layer is polycrystalline structure. SAED pattern shown in Figure 2c demonstrates the polycrystalline structures of Co(OH)$_2$/RGO/NiO SNTAs. The specific surface area was calculated by BET method on the basis of desorption branch of nitrogen sorption isotherms (Figure S4), and the Co(OH)$_2$/RGO/NiO SNTAs show a high BET specific surface area of 91.82 m^2 g^{-1}. The unique sandwich-like structure and highly void volume of Co(OH)$_2$/RGO/NiO SNTAs will allow that the electroactive species fully touch electrodes and the Co(OH)$_2$ and NiO layers will efficiently participate in the capacitive reactions.

XRD pattern of the Co(OH)$_2$/RGO/NiO SNTAs is shown in Figure 3a and it confirms the presence of crystalline Co(OH)$_2$ and NiO. The peak of RGO is not seen, and it also indicates that the RGO layer is amorphous. Raman spectroscopy is widely used for the characterization of electronic structure of carbon products, and here it is also used for RGO. Figure 3b shows Raman spectrum of Co(OH)$_2$/RGO/NiO SNTAs, and it shows the characteristic D and G bands at 1357 cm^{-1} and 1643 cm^{-1}. The D band is a common feature for sp^3 defects in carbon, and the G band provides information in plane vibrations of sp^2 bonded carbons. Compared with GO, the Co(OH)$_2$/RGO/NiO SNTAs show two differences in the Raman spectra. Firstly, the ratio I$_D$/I$_G$ of the Co(OH)$_2$/RGO/NiO SNTAs was much lower than that of GO, indicating a lower density of defects present in RGO.[37] Secondly, the G band shifts by ~31cm^{-1} as shown in Figure 3b. The blue-shifts of D and G bands can be attributed to the conversion of GO to RGO or the

resonance of isolated double bonds at higher frequencies.[37] Therefore, both the change in Raman band

intensity and blue shift of G band provide clear evidence for the presence of RGO in the composites.

XPS spectra of the $Co(OH)_2$/RGO/NiO SNTAs in C 1s region is shown in Figure 4a. The symmetric

C 1s peak at 284.78 eV is clearly seen for C-C bond, and it also demonstrates the existence of RGO.

Additionally, the oxygen functionalities attached to the carbons show a small deconvoluted peak of C-O

(285.3 eV) at a higher binding energy, indicating the existence of small amounts of oxygenated carbon

species in the RGO. This means that the oxygen functionalities can act as a special node to covalently

bond Co atoms and Ni atoms, greatly improving the binding power between $Co(OH)_2$, NiO and RGO.

To investigate the effects of RGO on electron structures of $Co(OH)_2$ and NiO, XPS spectra of the

$Co(OH)_2$/RGO/NiO SNTAs in Co 2p and Ni 2p regions were measured. Figure 4b shows XPS spectrum

of Co 2p of $Co(OH)_2$/RGO/NiO SNTAs. There are two main Co 2p peaks that locate at binding energy

of 797.0 eV (Co $2p_{1/2}$) and 781.1 eV (Co $2p_{3/2}$), respectively, with satellite peaks. The positions of Co 2p

peaks and the distance between two Co 2p peaks (ΔE_b=15.9 eV) indicate that the element Co exists as

$Co(OH)_2$ state.[38] In addition, we find that the binding energy of Co 2p for $Co(OH)_2$/RGO/NiO SNTAs

shows a positive shift of ~0.70 eV in relative to that of $Co(OH)_2$ NTAs (Figure S5a), indicating the

change of electronic states of Co atoms in the $Co(OH)_2$/RGO/NiO SNTAs. The Ni 2p XPS spectrum in

Figure 4c also exhibits two characteristic peaks at 855.9 and 873.6 eV, corresponding to Ni $2p_{3/2}$ and Ni

$2p_{1/2}$ spin-orbit peaks of NiO,[39] respectively, confirming the presence of NiO in the composite. The Ni

2p peaks of $Co(OH)_2$/RGO/NiO SNTAs shift ~0.50 eV to higher binding energy relative to those of NiO

NTAs (Figure S5b), indicating the change of electronic state of Ni atoms in $Co(OH)_2$/RGO/NiO SNTAs.

Therefore, the above shifts of Co 2p and Ni 2p in binding energies confirm the electron interactions

among the $Co(OH)_2$, NiO and RGO in $Co(OH)_2$/RGO/NiO SNTAs.

The role of RGO for the conductibility enhancement of $Co(OH)_2$/RGO/NiO SNTAs is studied by EIS

measurement. The Nyquist plot of $Co(OH)_2$@RGO@NiO SNTAs between 1 Hz and 10 kHz is shown in

Figure 5a, and the equivalent circuit of Nyquist plot is shown in Figure S6, where R_s is the solution

resistance, C_{dl} is a double-layer capacitor, R_{ct} is the charge transfer resistance, R_w is the Warburg

8

impedance, and C_L is the limit pseudocapacitor. Based on the results shown in Figure 5a, the Co(OH)$_2$/RGO/NiO SNTAs show much smaller R_{ct} compared with Co(OH)$_2$/NiO NTAs, indicating that the RGO layers can obviously reduce charge transfer resistance, thus improving the transport and collection of electrons in electrode. The enhanced conductibility of the Co(OH)$_2$/RGO/NiO SNTAs will favor rate capability for high power performance and fast charge-discharge. The utilization rate of electrode will also be largely enhanced by the high conductibility of electrode because of slight polarization. In addition, the Co(OH)$_2$/RGO/NiO SNTAs show steeper slop than the Co(OH)$_2$/NiO NTAs in Warburg area, indicating faster ion diffusion through the Co(OH)$_2$/RGO/NiO SNTAs. This can be attributed to larger surface area of Co(OH)$_2$/ RGO/NiO SNTAs than that of Co(OH)$_2$/NiO NTAs.

The supercapacitive performance of the Co(OH)$_2$/RGO/NiO SNTAs was firstly evaluated by cyclic voltammetry measurement in 1.0 mol·L^{-1} KOH aqueous solution using the half-cell test (a three-electrode configuration). Figure 5b shows cyclic voltammograms (CVs) of Co(OH)$_2$ NTAs, NiO NTAs, RGO NTAs, and Co(OH)$_2$/RGO/NiO SNTAs among the different window potentials at scan rate of 100 mV·s^{-1}. For Co(OH)$_2$ NTAs, NiO NTAs and Co(OH)$_2$/RGO/NiO SNTAs, the CVs all show symmetrical cathodic and anodic peaks. The results reflect good pseudocapacitance behaviors of Co(OH)$_2$, NiO and Co(OH)$_2$/NiO composite. The C_{sp} of Co(OH)$_2$/RGO/NiO SNTAs at 100 mV·s^{-1} is calculated to be 1093 F·g^{-1}, which is much larger than 332 F·g^{-1} of Co(OH)$_2$ NTAs, 221 F·g^{-1} of NiO NTAs and 155 F·g^{-1} of RGO NTAs at the same scan rate. When the scan rate is 5 mV·s^{-1}, the C_{sp} of Co(OH)$_2$/RGO/NiO SNTAs can achieve 1470 F·g^{-1}. Various CVs of Co(OH)$_2$/RGO/NiO SNTAs among -0.4~0.6 V at scan rates of 5~100 mV s^{-1} are shown in Figure 5c and the dependence of C_{sp} of Co(OH)$_2$/RGO/NiO SNTAs on scan rate is shown in Figure 5d. With scan rate increasing from 5 to 100 mV·s^{-1}, the Co(OH)$_2$/RGO/NiO SNTAs only show C_{sp} decay of about 25.6%, which is much smaller than 50.2% of C_{sp} decay of Co(OH)$_2$ NTAs and 48.3% of C_{sp} decay of NiO NTAs and is also much smaller than 57.3% of C_{sp} decay of RGO NTAs. Therefore, the above results show that the Co(OH)$_2$/RGO/NiO SNTAs own a much larger C_{sp} and a much better rate capability than Co(OH)$_2$ NTAs, NiO NTAs and RGO NTAs because of the special synergistic effects in the hybrid multi-layered Co(OH)$_2$/RGO/NiO SNTAs.

The influence of the composition on the electrochemical performance of $Co(OH)_2$/RGO/NiO SNTAs was evaluated. Firstly, the influence of RGO content on the electrochemical performance of $Co(OH)_2$/RGO/NiO SNTAs was studied as shown in Figure S7. With RGO content increasing from 2 at% to 12 at%, the C_{sp} of $Co(OH)_2$/RGO/NiO SNTAs first increases from 921 to 1470 $F \cdot g^{-1}$ at 5 $mV \cdot s^{-1}$ and then decreases to 1123 $F \cdot g^{-1}$. The low content of RGO in hybrid SNTAs causes the decrease of C_{sp} and this can be attributed to the poor conductivity of electrode. When the RGO content is 6 at%, the $Co(OH)_2$/RGO/NiO SNTAs show the largest C_{sp} of 1470 $F \cdot g^{-1}$ at 5 $mV \cdot s^{-1}$. However, when the RGO content increases to 12 at%, the C_{sp} of $Co(OH)_2$/RGO/NiO SNTAs decreases to 1103 $F \cdot g^{-1}$. This can be attributed to the electrochemical double layer behavior of RGO and the C_{sp} of RGO is smaller than those of $Co(OH)_2$ and NiO. In addition, the influence of $Co(OH)_2$: NiO ratio in the SNTAs on electrochemical performance was evaluated as shown in Figure S8 (1:1, 1:2, 1:3, 2:1, and 3:1 mole ratios of $Co(OH)_2$/NiO and the content of RGO is fixed to 6 at%). The 1:1 mole ratio of $Co(OH)_2$: NiO in the $Co(OH)_2$/RGO/NiO SNTAs shows the largest C_{sp}, indicating the favorable mole ratio of $Co(OH)_2$: NiO in the SNTAs is 1:1.

Galvanostatic charge-discharge curves of the $Co(OH)_2$/RGO/NiO SNTAs (the mole ratio of $Co(OH)_2$: RGO : NiO is 47 : 6 : 47 and it is fixed for all following studies) in the half-cell system at various current densities are shown in Figure 6a, which shows a symmetric nature in the charging/discharging curves, indicating good supercapacitive characteristic and superior reversible redox reactions. When the current density is 2.0 $A \cdot g^{-1}$, the $Co(OH)_2$/RGO/NiO SNTAs achieve a C_{sp} of 1507 $F \cdot g^{-1}$. Figure 6b shows the summary plot of C_{sp} *vs* current density, which also demonstrates that the $Co(OH)_2$/RGO/NiO SNTAs exhibit significantly enhanced supercapacitive performance compared with $Co(OH)_2$ NTAs, NiO NTAs and RGO NTAs. With charging/discharging rate increasing from 2.0 to 32 $A \cdot g^{-1}$, the $Co(OH)_2$/RGO/NiO SNTAs only show ~33.6% C_{sp} loss, which is much smaller than 52.4% of $Co(OH)_2$ NTAs, 64.5% of NiO NTAs, and 68.1% of RGO NTAs. So the above result also demonstrates that the $Co(OH)_2$/RGO/NiO SNTAs have a much higher C_{sp} and a much better rate capability than $Co(OH)_2$ NTAs, NiO NTAs and RGO NTAs at different current densities.

Nanoscale Accepted Manuscript

The Co(OH)$_2$/RGO/NiO SNTAs show excellent long-term cycling stability in the half-cell system, and this is very important for the practical operations. The C_{sp} variation of Co(OH)$_2$/RGO/NiO SNTAs as a function of cycle number at 4.5 A·g^{-1} is shown in Figure 6c, which shows the Co(OH)$_2$/RGO/NiO SNTAs almost can withstand over 10,000 cycles without any significant decrease in C_{sp}. After 10,000 cycles, the C_{sp} retention of Co(OH)$_2$/RGO/NiO SNTAs still keep ~98%. However, after 10,000 cycles, the Co(OH)$_2$ NTAs, NiO NTAs and RGO NTAs only show C_{sp} retention of ~68%, 66% and 42%, respectively. The above results demonstrate that the Co(OH)$_2$/RGO/NiO SNTAs as electrodes own much higher cycling stability than Co(OH)$_2$ NTAs, NiO NTAs and RGO NTAs. The cycling performance of the Co(OH)$_2$/RGO/NiO SNTAs at progressively increased and decreased current density is also studied and it is shown in Figure 6d, which shows the Co(OH)$_2$/RGO/NiO SNTAs still own high cycling stability after the electrode suffered from sudden current density change. Therefore, the combination of Co(OH)$_2$, RGO, and NiO into the unique SNTAs not only enhance C_{sp} but also highly improve the long-term cycling stability.

To investigate the practical application of Co(OH)$_2$/RGO/NiO SNTAs, here the asymmetric supercapacitors (ASCs) were assembled by using Co(OH)$_2$/RGO/NiO SNTAs as positive electrode and active carbon (AC) as negative electrode (the AC electrode was evaluated as shown in Figure S9 in Supporting Information, and it is a good candicate as negative electrode). To determine the best operating potential of ASCs, the CVs of Co(OH)$_2$/RGO/NiO SNTAs (green curve) and AC electrode (black curve) were measured in 1.0 mol·L^{-1} KOH solution, respectively, and they are shown in Figure S10. The voltage windows of Co(OH)$_2$/RGO/NiO SNTAs and AC electrodes were complementarity, and they are good candidates for the ASCs. Here we found the operating potentials of the ASCs device could been chosen from 0 to 1.6 V. CVs of the ASCs device at 100 mV·s^{-1} were measured in 1.0 mol·L^{-1} KOH solution as shown in Figure S11. It should be noted that the calculated C_{sp} of ASCs was based on the total weight of positive and negative electrodes because it is not meaningful to deduce the C_{sp} of a single electrode. The C_{sp} of Co(OH)$_2$/RGO/NiO SNTAs//AC ASCs at 100 mV·s^{-1} is calculated to be 130 F·g^{-1}, which is much larger than those of Ni$_x$Co$_{3-x}$O$_4$//AC ASCs (<50 F·g^{-1}),[40] RGO/PPy//AC ASCs (<65

F·g^{-1}),[41] Co(OH)$_2$//VN ASCs (<95 F·g^{-1}),[42] CNT-CM//ACNF ASCs (<35 F·g^{-1})[43] and Bi$_2$O$_3$//AC ASCs

(<30 F·g^{-1})[44] at the same scan rate. Galvanostatic charge-discharge curves of the Co(OH)$_2$/RGO/NiO

SNTAs//AC ASCs at various current densities are shown in Figure 7a. The C_{sp} of Co(OH)$_2$/RGO/NiO

SNTAs//AC ASCs at current density of 2.5 A·g^{-1} is calculated to be 321 F·g^{-1}, which is larger than those

of RGO/PPy//AC ASCs (58 F·g^{-1}),[41] PEDOT/A-CNT//graphene (42 F·g^{-1}),[45] CFP/PPy//RGO/MWCNT

ASCs (70 F·g^{-1}),[46] Co$_3$O$_4$/RGO//AC ASCs (108 F·g^{-1}),[47] GH//MnO$_2$-NF ASCs (<40 F·g^{-1}),[48] Ni$_x$Co$_{1-x}$

LDH-ZTO//AC ASCs (<100 F·g^{-1}),[49] UPMNFs//FMCNTs ASCs (<20 F·g^{-1}),[50] and Bi$_2$O$_3$//AC ASCs

(<30 F·g^{-1})[44] at the same current density. With charging/discharging rate increasing from 2.5 to 36 A·g^{-1},

the Co(OH)$_2$/RGO/NiO SNTAs//AC ASCs only show ~31.4% C_{sp} loss as shown in Figure 7b, indicating

a good rate performance.

Another important requirement for supercapacitor application is cycling stability. The C_{sp} variation of

the Co(OH)$_2$/RGO/NiO SNTAs//AC ASCs as a function of cycle number at a current density of 2.5 A·g^{-1}

is shown in Figure 7c, which shows the Co(OH)$_2$/RGO/NiO SNTAs//AC ASCs almost can withstand

over 10,000 cycles without significant decrease in C_{sp} value. After 10,000 cycles, the C_{sp} retention of the

Co(OH)$_2$/RGO/NiO SNTAs//AC ASCs keeps about 95%. The above results well demonstrate that the

Co(OH)$_2$/RGO/NiO SNTAs//AC ASCs own superior cycling stability.

The energy and power densities of Co(OH)$_2$/RGO/NiO SNTAs//AC ASCs are also studied because

they are highly important for electrochemical devices. The Ragone plot (power density *vs* energy density)

at various current densities is shown in Figure 7d, which shows the Co(OH)$_2$/RGO/NiO SNTAs//AC

ASCs can deliver a maximum energy density of ~115 Wh·kg^{-1} at 2.5 A·g^{-1} and the maximum power

density of ~27.5 kW·kg^{-1} at 36 A·g^{-1}, which are much superior to those of Co(OH)$_2$ NTAs//AC ASCs

(46 Wh·kg^{-1} and 15 kW·kg^{-1}) and NiO NTAs//AC ASCs (32 Wh·kg^{-1} and 11 kW·kg^{-1}). More importantly,

the obtained maximum energy density is considerably larger than those of recently reported many ASCs

at the same current density, such as sGNS/cMWCNT/PANI//aGNS ASCs (<45 Wh·kg^{-1}),[51]

Ni(OH)$_2$/graphene//porous graphene ASCs (<13.5 Wh·kg^{-1}),[52] MnO$_2$//graphene hydrogel ASCs (<14.9

Wh·kg^{-1}),[53] MnO$_2$//mesoporous carbon nanotubes ASCs (<10.4 Wh·kg^{-1}),[54] graphene/MnO$_2$//activated

carbon nanofiber ASCs (<8.2 Wh·kg^{-1}),[55] activated carbon//K$_{0.27}$MnO$_2$·0.6H$_2$O ASCs (<17.6 Wh·kg^{-1}),[56]

GH//MnO$_2$-NF ASCs (<23.2 Wh·kg^{-1}),[48] MnO$_2$//AC ASCs (<30.0 Wh·kg^{-1}),[57] and Ni(OH)$_2$/CNT-AC

ASCs (<50.6 Wh·kg^{-1}).[58] Furthermore, the maximum power density of Co(OH)$_2$/RGO/NiO SNTAs//AC

ASCs also is higher than those of above mentioned ASCs as shown in Figure 7d. Here the highest power

density, 27.5 kW·kg^{-1}, can adequately meet the power demand of PNGV (Partnership for a New

Generation of Vehicles), 15 kW·kg^{-1}, demonstrating the excellent capability of the Co(OH)$_2$/RGO/NiO

SNTAs//AC ASCs as power supply components in hybrid vehicle systems.

4. CONCLUSIONS

In summary, the novel Co(OH)$_2$/RGO/NiO SNTAs were fabricated by ZnO template-assisted

electrodeposition and they exhibited significantly enhanced electrochemical performance as compared

to Co(OH)$_2$ NTAs, RGO NTAs and NiO NTAs. The Co(OH)$_2$/RGO/NiO SNTAs electrode shows a high

C_{sp} of 1470 F·g^{-1} at 5 mV·s^{-1} and superior rate capability with 25.6% C_{sp} decay from 5 to 100 mV·s^{-1}.

Furthermore, the Co(OH)$_2$/RGO/NiO SNTAs electrode exhibits excellent cycling performance with 98%

C_{sp} retention after 10,000 cycles. The significant improvement of the electrochemical performance of

Co(OH)$_2$/RGO/NiO SNTAs can be attributed to the special surface morphology of SNTAs and

synergistic effects among Co(OH)$_2$, RGO, and NiO. The high-performance ASCs were assembled by

using Co(OH)$_2$/RGO/NiO SNTAs as positive electrode and AC as negative electrode, and they could

operate in a wide voltage window of 1.6 V. The assembled ASCs delivered a maximum energy density

of 115 Wh·kg^{-1}, a maximum power density of 27.5 kW·kg^{-1}, and excellent cycling performance (<5%

C_{sp} loss after 10,000 cycles). This work shows an important breakthrough in the design and fabrication

of high-performance multi-walled hybrid SNTAs for electrochemical energy storage.

ASSOCIATED CONTENT

Supporting Information

SEM images, XPS spectra, equivalent circuit, and CVs. This material is available free of charge via the

Internet at http://pubs.rsc.org.

Nanoscale Accepted Manuscript

AUTHOR INFORMATION

Corresponding Author

ligaoren@mail.sysu.edu.cn

Notes

The authors declare no competing financial interest.

ACKNOWLEDGMENTS

REFERENCES

(1) L.-F. Chen, Z.-H. Huang, H.-W. Liang, Q.-F. Guan, S.-H. Yu, *Adv. Mater.* 2013, **25**, 4746-4752.

(2) J. Feng, X. Sun, C. Wu, L. Peng, C. Lin, S. Hu, J. Yang, Y. Xie, *J. Am. Chem. Soc.* 2011, **133**, 17832-17838.

(3) Y. Yang, Z. Peng, G. Wang, G. Ruan, X. Fan, L. Li, H. Fei, R. H. Hauge, J. M. Tour, *ACS Nano* 2014, **8**, 7279-7287.

(4) L.-F. Chen, X.-D. Zhang, H.-W. Liang, M. Kong, Q.-F. Guan, P. Chen, Z.-Y. Wu, S.-H. Yu, *ACS Nano* 2012, **6**, 7092-7102.

(5) L. L. Zhang, X. Zhao, M. D. Stoller, Y. Zhu, H. Ji, S. Murali, Y. Wu, S. Perales, B. Clevenger, R. S. Ruoff, *Nano Lett.* 2012, **12**, 1806-1812.

(6) L. Peng, X. Peng, B. Liu, C. Wu, Y. Xie, G. Yu, *Nano Lett.* 2013, **13**, 2151-2157.

(7) L. Yu, L. Zhang, H. B. Wu, X. W. Lou, *Angew. Chem. Int. Ed.* 2014, **53**, 3711-3714.

(8) S. Li, D. Wu, C. Cheng, J. Wang, F. Zhang, Y. Su, X. Feng, *Angew. Chem. Int. Ed.* 2013, **52**, 12105-12109.

(9) Z. Weng, F. Li, D.-W. Wang, L. Wen, H.-M. Cheng, *Angew. Chem. Int. Ed.* 2013, **52**, 3722-3725.

(10) L.-F. Chen, Z-Y. Yu, X. Ma, Z.-Y. Li, S.-H. Yu, *Nano Energy* 2014, **9**, 345-354.

(11) J. Kang, A. Hirata, H.-J. Qiu, L. Y. Chen, X. B. Ge, T. Fujita, M. W. Chen, *Adv. Mater.* 2014, **26**, 269-272.

(12) Y. Meng, K. Wang, Y. Zhang, Z. Wei, *Adv. Mater.* 2013, **25**, 6985-6990.

(13) Z. Niu, L. Zhang, L. Liu, B. Zhu, H. Dong, X. Chen, *Adv. Mater.* 2013, **25**, 4035-4042.

(14) T. Chen, Y. Xue, A. K. Roy, L. Dai, *ACS Nano* 2014, **8**, 1039-1046.

(15) G. Zhang, X. W. Lou, *Adv. Mater.* 2013, **25**, 976-979.

(16) J. Liu, J. Jiang, C. Cheng, H. Li, J. Zhang, H. Gong, H. J. Fan, *Adv. Mater.* 2011, **23**, 2076-2081.

(17) Z.-L. Wang, R. Guo, G.-R. Li, H.-L. Lu, Z.-Q. Liu, F.-M. Xiao, M. Zhang, Y.-X. Tong, *J. Mater. Chem.* 2012, **22**, 2401-2404**.**

(18) J. Yan, A. Sumboja, E. Khoo, P. S. Lee, *Adv. Mater.* 2011, **23**, 746-750.

(19) T.-Y. Wei, C.-H. Chen, H.-C. Chien, S.-Y. Lu, C.-C. Hu, *Adv. Mater.* 2010, **22**, 347-351.

(20) J. Yan, Z. Fan, W. Sun, G. Ning, T. Wei, Q. Zhang, R. Zhang, L. Zhi, F. Wei, *Adv. Funct. Mater.* 2012, **22**, 2632-2641.

(21) Q. Qu, Y. Zhu, X. Gao, Y. Wu, *Adv. Energy Mater.* 2012, **2**, 950-955.

(22) Q. Lu, M. W. Lattanzi, Y. Chen, X. Kou, W. Li, X. Fan, K. M. Unruh, J. G. Chen, J. Q. Xiao, *Angew. Chem. Int. Ed.* 2011, **50**, 6847-6850.

(23) S. Gao, Y. Sun, F. Lei, L. Liang, J. Liu, W. Bi, B. Pan, Y. Xie, *Angew. Chem. Int. Ed.* 2014, **53**, DOI: 10.1002/anie.201407836.

(24) D. Chao, X. Xia, C. Zhu, J. Wang, J. Liu, J. Lin, Z. Shen, H. J. Fan, *Nanocale* 2014, **6**, 5691-5697.

(25) J. Luo, J. Liu, Z. Zeng, C. F. Ng, L. Ma, H. Zhang, J. Lin, Z. Shen, H. J. Fan, *Nano Lett.* 2013, **13**, 6136-6143.

(26) S. Hou, G. Zhang, W. Zeng, J. Zhu, F. Gong, F. Li, H. Duan, *ACS Appl. Mater. Interfaces* 2014, **6**, 13564-13570.

(27) J. Xu, Q. Wang, X. Wang, Q. Xiang, B. Liang, D. Chen, G. Shen, *ACS Nano* 2013, **7**, 5453-5462.

(28) X. Xia, D. Chao, Z. Fan, C. Guan, X. Cao, H. Zhang, H. J. Fan, *Nano Lett.* 2014, **14**, 1651-1658.

(29) X. Liu, P. Shang, Y. Zhang, X. Wang, Z. Fan, B. Wang, Y. Zheng, *J. Mater. Chem. A* 2014, **2**, 15273-15278.

(30) J. Xu, F. He, S. Gai, S. Zhang, L. Li, P. Yang, *Nanoscale* 2014, **6**, 10887-10895.

(31) H. Wang, H. S. Casalongue, Y. Liang, H. Dai, *J. Am. Chem. Soc.* 2010, **132**, 7472-7477.

(32) (a) G. Zhang, B. Y. Xia, C. Xiao, L. Yu, X. Wang, Y. Xie, X. W. Lou, *Angew. Chem. Int. Ed.* 2013, **52**, 8643-8647. (b) X. Xu, B. Dong, S. Ding, C. Xiao, D. Yu, *J. Mater. Chem. A* 2014, **2**, 13069-13074.

(33) S. Zhuo, Y. Xu, W. Zhao, J. Zhang, B. Zhang, *Angew. Chem. Int. Ed.* 2013, **52**, 8602-8606.

(34) J. Liang, Z. Fan, S. Chen, S. Ding, G. Yang, *Chem. Mater.* 2014, **26**, 4354-4360.

(35) H. T. Tan, X. Rui, H. Yu, W. Liu, C. Xu, Z. Xu, H. H. Hng, Q. Yan, *ACS Nano* 2014, **8**, 4004-4014.

(36) J. Zhao, J. Chen, S. Xu, M. Shao, Q. Zhang, F. Wei, J. Ma, M. Wei, D. G. Evans, X. Duan, *Adv. Funct. Mater.* 2014, **24**, 2938-2946.

(37) (a) Y. Xue, B. Wu, L. Jiang, Y. Guo, L. Huang, J. Chen, J. Tan, D. Geng, B. Luo, W. Hu, G. Yu, Y. Liu, *J. Am. Chem. Soc.* 2012, **134**, 11060-11063. (b) S. D. Perera, R. G. Mariano, K. Vu, N. Nour, O. Seitz, Y. Chabal, J. K. J. Balkus, *ACS Catal.* 2012, **2**, 949-956.

(38) T. Xue, X. Wang, J.-M. Lee, *J. Power Sources* 2012, **201**, 382-386.

(39) D. T. Dam, X. Wang, J.-M. Lee, *ACS Appl. Mater. Interfaces* 2014, **6**, 8246-8256.

(40) R. Wang, X. Yan, *Sci. Rep.* **2013**, *4*, 3712.

(41) L.-Q. Fan, G.-J. Liu, J.-H. Wu, L. Liu, J.-M. Lin, Y.-L. Wei, *Electrochim. Acta* 2014, **137**, 26-33.

(42) R. Wang**,** X. Yan**,** J. Lang**,** Z. Zheng, P. Zhang, *J. Mater. Chem. A* 2014, **2**, 12724-12732.

(43) J.-G. Wang, Y. Yang, Z.-H. Huang, F. Kang, *Carbon* 2013, **61**, 190-199.

(44) S. T. Senthilkumar, R. K. Selvan, M. Ulaganathan, J. S. Melo, *Electrochim. Acta* 2014, **115**, 518-524.

(45) Y. Zhou, N. Lachman, M. Ghaffari, H. Xu, D. Bhattacharya, P. Fattahi, M. Abidian, S. Wu, K. K. Gleason, B. L. Wardle, Q. M. Zhang, *J. Mater. Chem. A* 2014, **2**, 9964-9969.

(46) C. Yang, J. Shen, C. Wang, H. Fei, H. Bao, G. Wang, *J. Mater. Chem. A* 2014, **2**, 1458-1464.

(47) L.-J. Xi, J.-F. Wu, C.-M. Chen, C.-M. Zhang, L. Wan, J.-L. Wang, Q.-Q. Kong, C.-X. Lv, K.-X. Li, G.-H. Sun, *J. Power Sources* 2013, **242**, 148-156.

(48) H. Gao, F. Xiao, C. B. Ching, H. Duan, *ACS Appl. Mater. Interfaces* 2012, **4**, 2801-2810.

(49) X. Wang, A. Sumboj, M. Lin, J. Yan, P. S. Lee, *Nanoscale* 2012, **4**, 7266-7272.

(50) H. Jiang, C. Li, T. Sun, J. Ma, *Nanoscale* 2012, **4**, 807-812.

(51) J. Shen, C. Yang, X. Li, G. Wang, *ACS Appl. Mater. Interfaces* 2013, **5**, 8467-8476.

(52) J. Yan, Z. J. Fan, W. Sun, G. Q. Ning, T. Wei, Q. Zhang, R. F. Zhang, L. J. Zhi, F. Wei, *Adv. Funct. Mater.* 2012, **22**, 2632-2641.

(53) H. C. Gao, F. Xiao, C. B. Ching, H. W. Duan, *ACS Appl. Mater. Interfaces* 2012, **4**, 2801-2810.

(54) H. Jiang, C. Z. Li, T. Sun, J. Ma, *Nanoscale* 2012, **4**, 807-812.

(55) Z. J. Fan, J. Yan, T. Wei, L. J. Zhi, G. Q. Ning, T. Y. Li, F. Wei, *Adv. Funct. Mater.* 2011, **21**, 2366-2375.

(56) Q. T. Qu, L. Li, S. Tian, W. L. Guo, Y. P. Wu, R. Holze, *J. Power Sources* 2010, **195**, 2789-2794.

(57) Q. Qu, P. Zhang, B. Wang, Y. Chen, S. Tian, Y. Wu, R. Holze, *J. Phys. Chem. C* 2009, **113***,* 14020-14027.

(58) Z. Tang, C. Tang, H. Gong, *Adv. Funct. Mater.* 2012, **22**, 1272-1278.
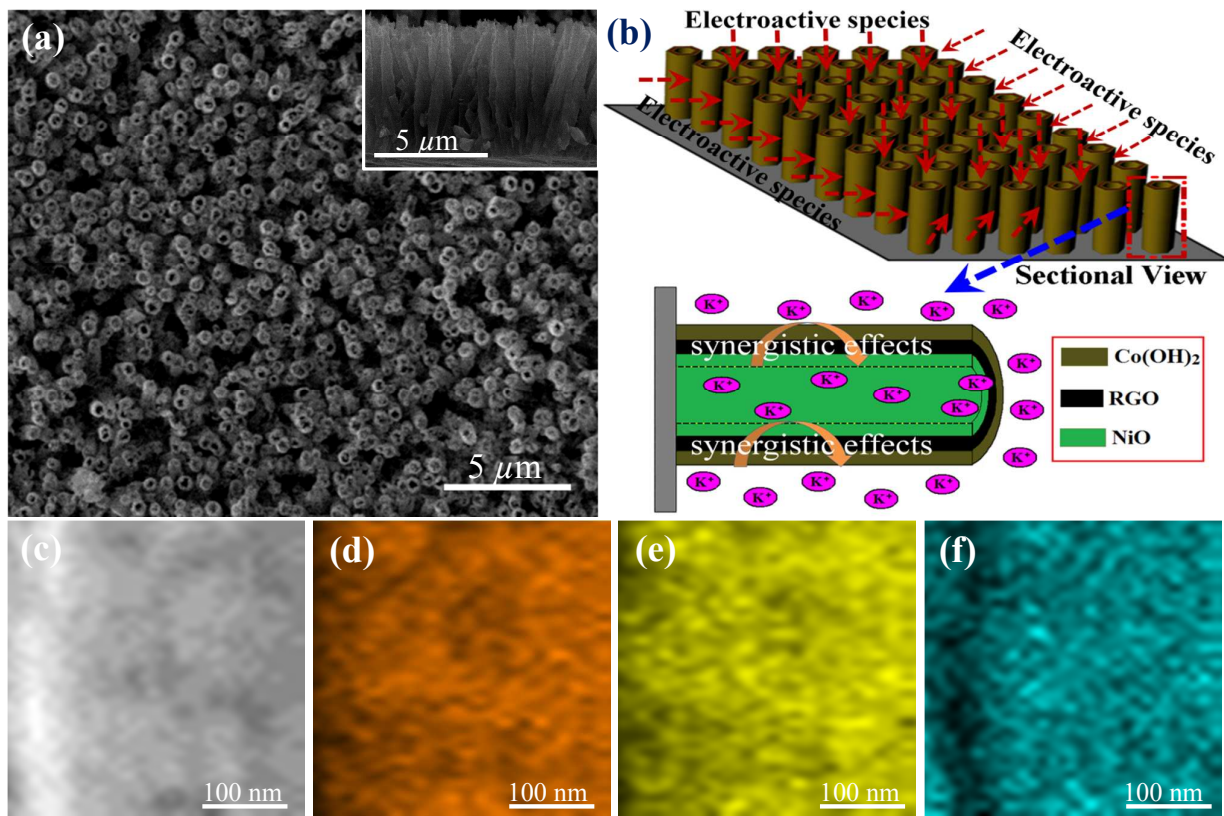
Figure 1. (a) SEM image of Co(OH)$_2$/RGO/NiO SNTAs (Inset is the sectional view); (b) Schematic illustration of the advantages of Co(OH)$_2$/RGO/NiO SNTAs as electrodes for SCs; (c) SEM image of the typical partial surface of Co(OH)$_2$/RGO/NiO SNTAs; EDS mappings measured on the partial surface: (d) Co mapping, (e) C mapping, and (f) Ni mapping.
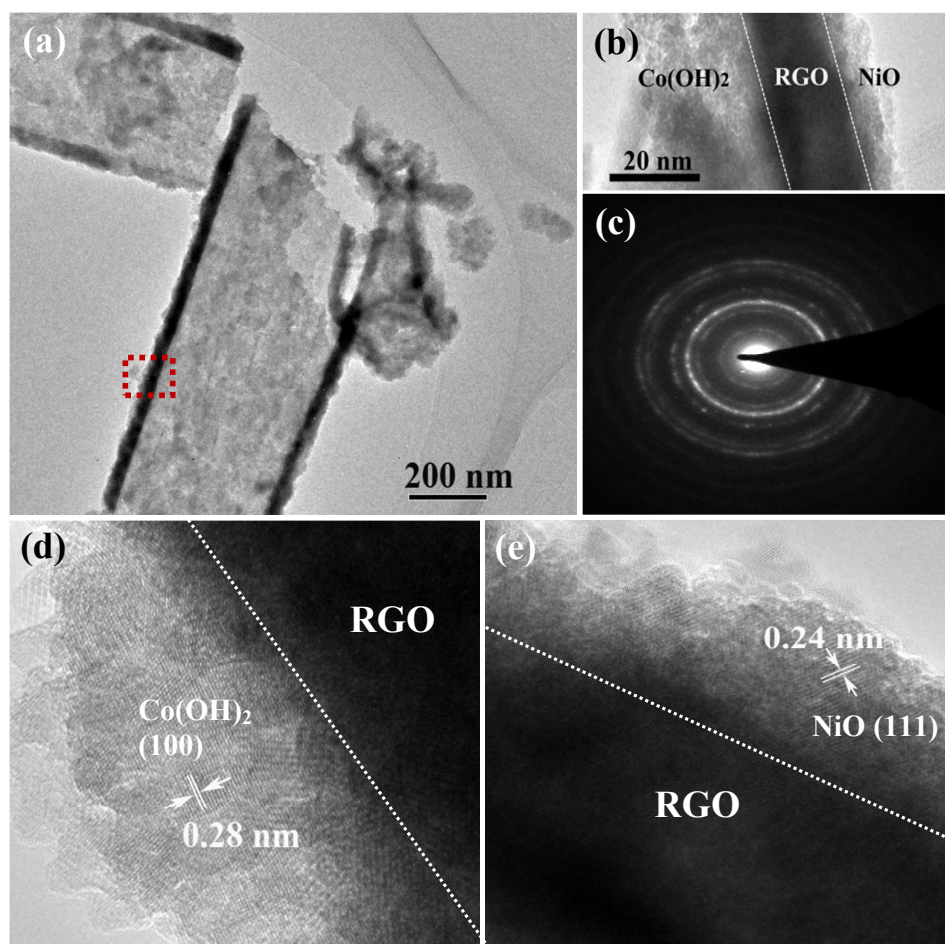
Figure 2. (a) TEM image of Co(OH)$_2$/RGO/NiO SNTAs; (b) The magnified TEM image of the wall of a typical Co(OH)$_2$/RGO/NiO nanotube; (c) SAED pattern of the wall of Co(OH)$_2$/RGO/NiO nanotube; (d) HRTEM image of Co(OH)$_2$/RGO interface; (e) HRTEM image of RGO/NiO interface.
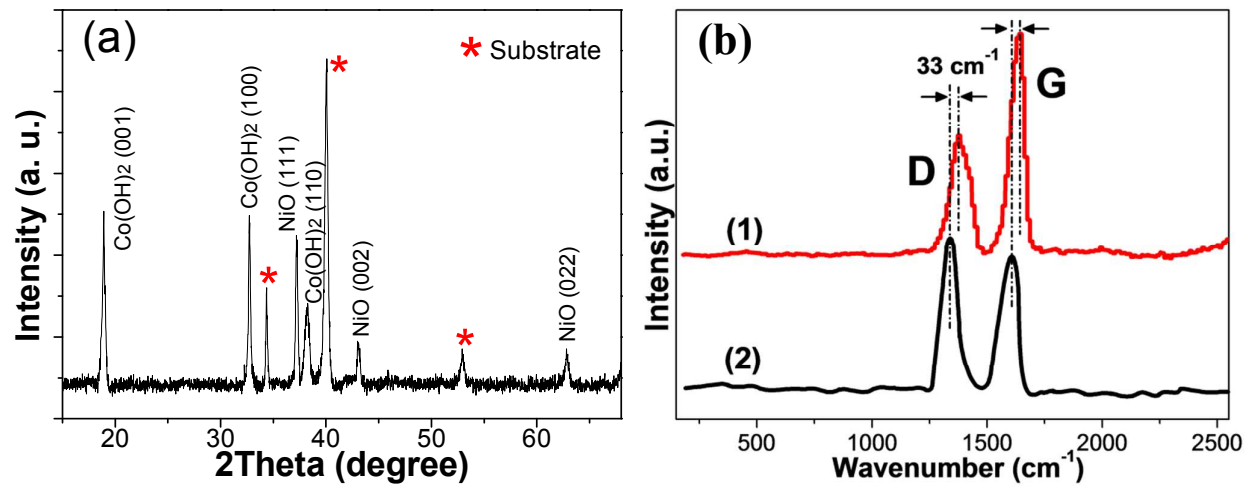
Figure 3. (a) XRD of Co(OH)$_2$/RGO/NiO SNTAs; (b) Raman spectra of (1) Co(OH)$_2$/RGO/NiO SNTAs
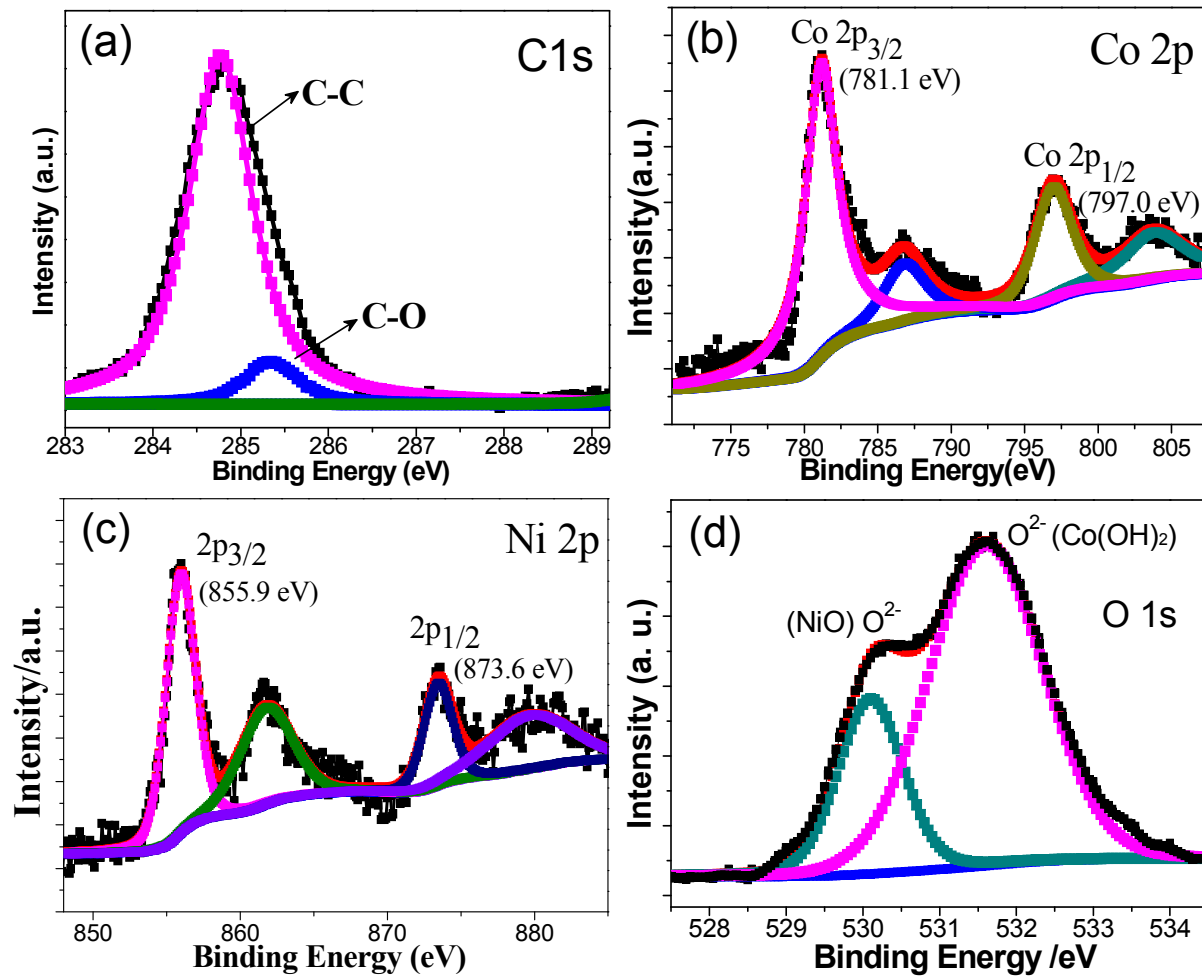
and (2) GO films.

Figure 4. XPS spectra of (a) C 1s, (b) Co 2p, (c) Ni 2p, and (d) O 1s performed on $Co(OH)_2$/RGO/NiO
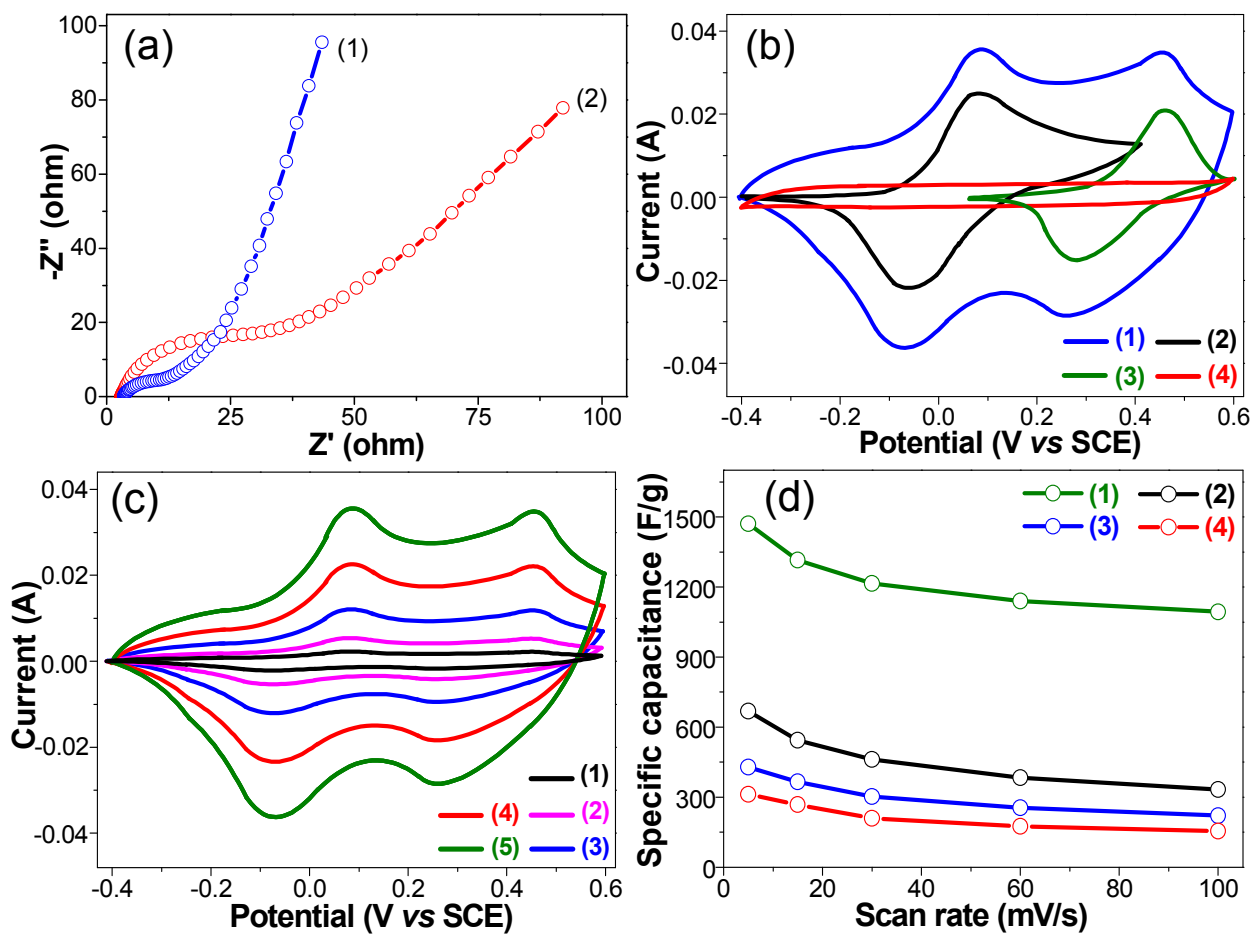
HNTAs.

Figure 5. (a) Nyquist plots of (1) Co(OH)$_2$/RGO/NiO SNTAs, (2) Co(OH)$_2$/NiO NTAs; (b) CVs of (1) Co(OH)$_2$/RGO/NiO SNTAs, (2) Co(OH)$_2$ NTAs, (3) NiO NTAs and (4) RGO NTAs at 100 mV/s; (c) CVs of Co(OH)$_2$/RGO/NiO SNTAs at different scan rates: (1) 5, (2) 10, (3) 30, (4) 60, (5) 100 mV/s; (d) The dependence of C_{sp} on scan rate for of (1) Co(OH)$_2$/RGO/NiO SNTAs, (2) Co(OH)$_2$ NTAs, (3) NiO NTAs and (4) RGO NTAs.
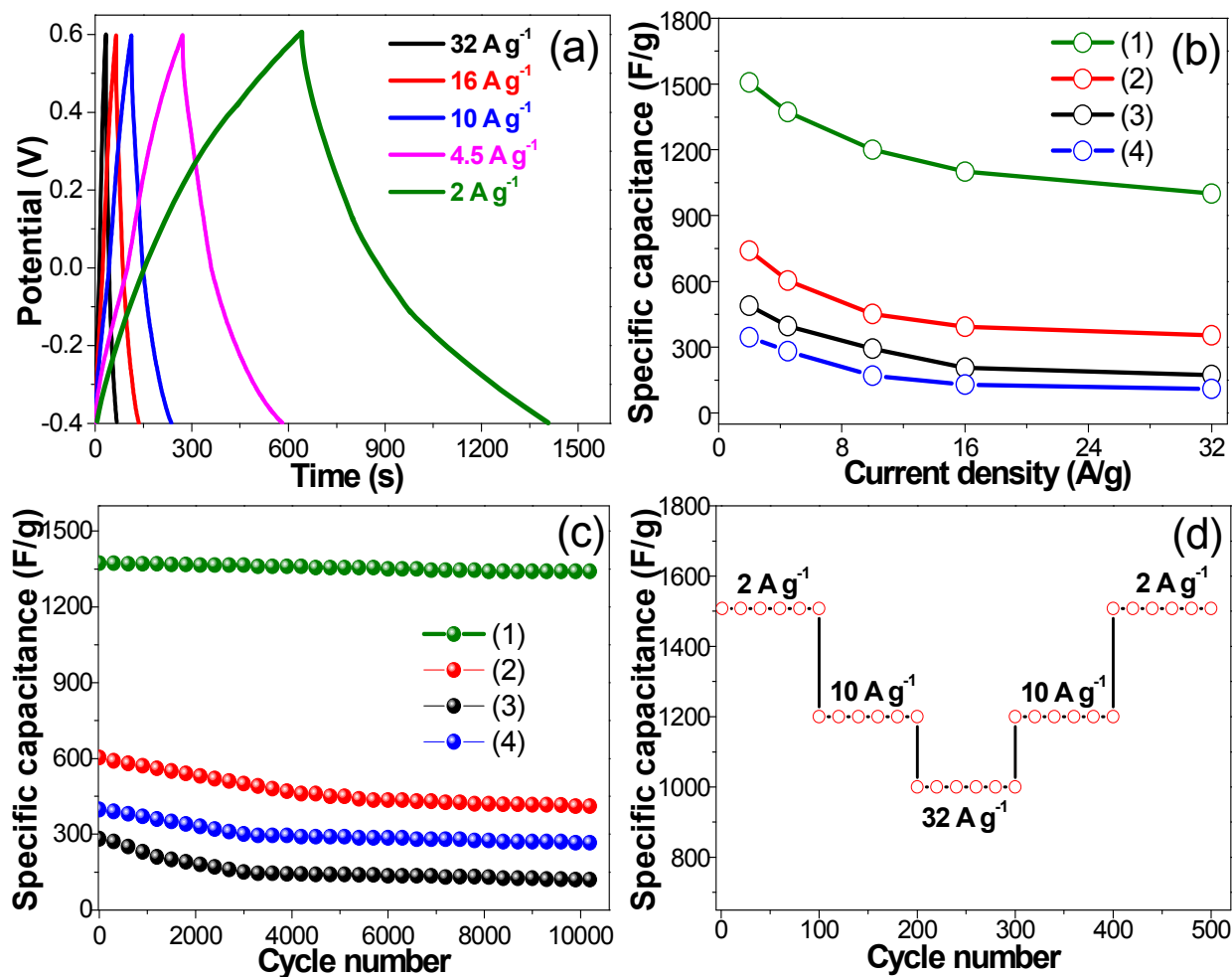
Figure 6. (a) Galvanostatic charge/discharge curves of Co(OH)$_2$/RGO/NiO SNTAs at different current

densities; (b) The dependence of C_{sp} on current density; (c) Cycle performance for 10,000 cycles at 4.5

A/g of (1) Co(OH)$_2$/RGO/NiO SNTAs, (2) Co(OH)$_2$ NTAs, (3) NiO NTAs and (4) RGO NTAs; (d)

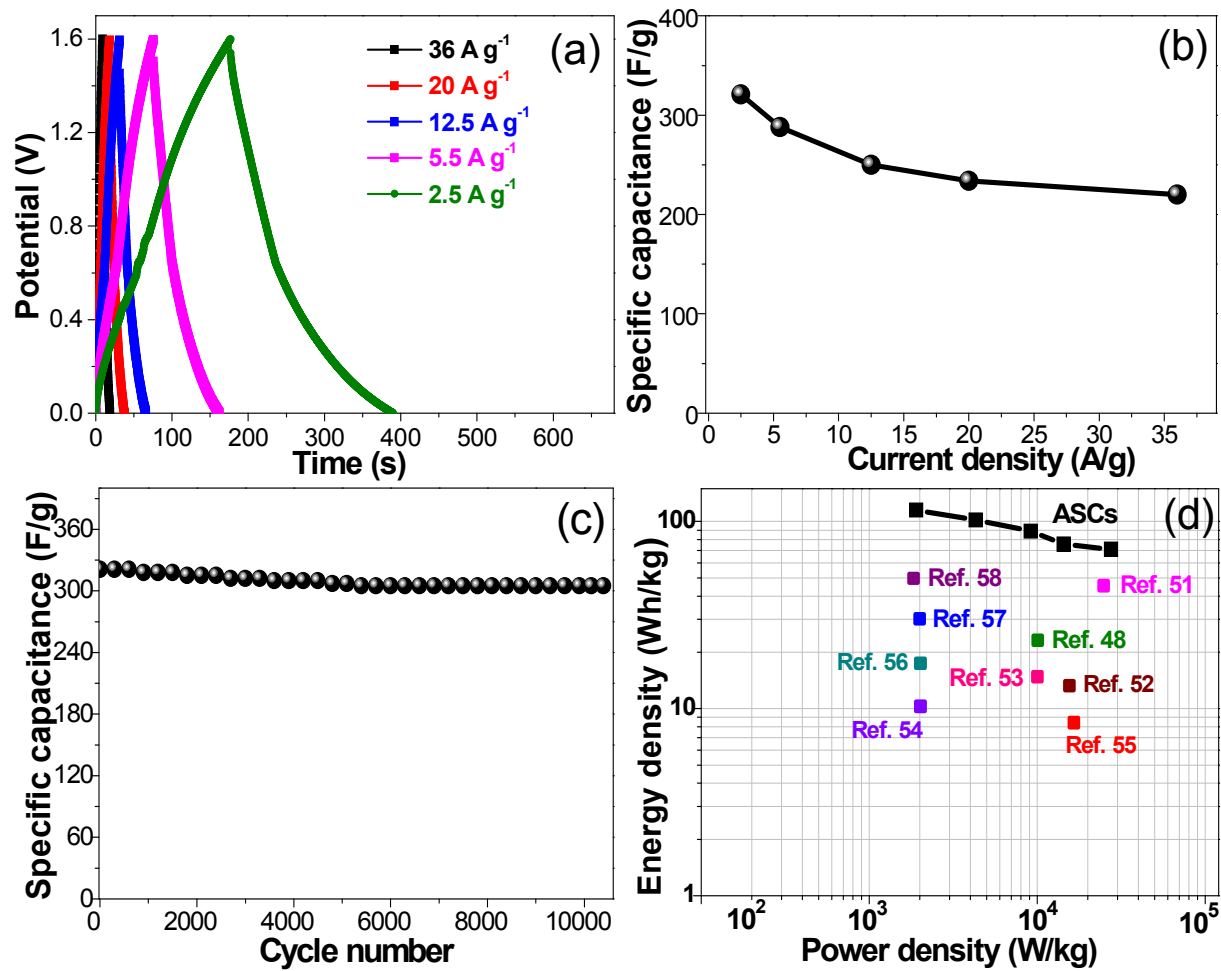Cycle life of Co(OH)$_2$/RGO/NiO SNTAs at progressively changed current densities.

Figure 7. (a) Galvanostatic charge/discharge curves of ASCs at different current densities; (b) The

dependence of C_{sp} on current density for ASCs; (c) Cycling performance of the ASC after 10,000 cycles

at 2.5 A/g; (d) Ragone plots of the ASC devices (The maximum energy densities and power densities

reported for other ASCs are added for comparison.[48,51-58])

TOC GRAPHICS